

# A Chimera method for high-fidelity simulation of turbulent flows

Andrea Di Mascio<sup>\*1</sup> and Sergio Pirozzoli<sup>†2</sup>

<sup>1</sup>Dipartimento di Ingegneria Industriale e dell'Informazione e di Economia, Università degli Studi dell'Aquila, Piazzale Ernesto Pontieri, Monteluco di Roio, 67100 L'Aquila, Italy

<sup>2</sup>Dipartimento di Ingegneria Meccanica e Aerospaziale, Sapienza Università di Roma, Via Eudossiana 18, 00184 Rome, Italy

June 9, 2025

## Abstract

We develop a block-structured solver for high-fidelity simulation of flows in complex geometries, based on overlapping (Chimera) meshes. The key components of the algorithm are a baseline dissipation-free central discretization and selective high-order filtering, which ensure uniform accuracy and minimal numerical diffusion. These favorable properties are preserved through efficient interpolation across overlapping blocks. Numerical tests demonstrate that the method guarantees a uniform order of accuracy even for distorted, overlapping meshes. Tests conducted for turbulent flow in a pipe show no significant issues at the interfaces or overlapping blocks, highlighting the method's potential for direct numerical simulation (DNS). Finally, we show that the method performs satisfactorily for geometrically complex problems, such as flow past a ship propeller, where it accurately replicates experimental data.

## 1 Introduction

Direct numerical simulation of turbulence (DNS) started several decades ago as a pioneering tool for the exploration of fundamental physical phenomena. Early studies (Orszag and Patterson, 1972; Kim et al., 1987) were limited to extremely simple geometries with periodic boundary conditions along two of three spatial directions, and to low Reynolds numbers corresponding to barely turbulent flow conditions. Over the years, DNS has mainly remained a tool to analyze relatively simple flows including homogeneous directions, although the accessible Reynolds numbers have greatly increased. As a recent example, turbulent flow in a circular pipe up to bulk Reynolds number ( $Re_b = Du_b/\nu$ , where  $u_b$  is the mean flow velocity,  $D$  is the pipe diameter, and  $\nu$  is the fluid kinematic viscosity)  $Re_b = 615,000$  has been reached, corresponding to typical operating conditions in oil pipelines (Pirozzoli, 2024).

The fast growth in accessible Reynolds numbers has been made possible by the exponential growth in the computing power of supercomputers, following Moore's law with good precision (<https://www.top500.com>). Progress on the side of geometrical complexity has not been as rapid, although flows of technological interest are starting to be approached (Hosseini et al., 2016). This shortcoming is mainly due to the fact that DNS requires computationally efficient algorithms,

---

<sup>\*</sup>Email: [andrea.dimascio@univaq.it](mailto:andrea.dimascio@univaq.it)

<sup>†</sup>Email: [sergio.pirozzoli@uniroma1.it](mailto:sergio.pirozzoli@uniroma1.it)

which are typically available only for simplified geometrical settings. Typical DNS algorithms rely on the use of Cartesian or curvilinear structured grids, which allow for high accuracy with excellent computational efficiency. However, flows with even moderate geometrical complexity cannot be easily accommodated on structured mesh systems.

The use of unstructured meshes is the natural alternative; however, computational efficiency here is severely hampered by memory stride related to the difficulty of efficiently storing arrays in the absence of natural data ordering. A possible alternative to the use of unstructured meshes involves the so-called Chimera approach, first introduced for the Euler equations by Benek et al. (1983). In essence, the method involves the use of one (or more) body-fitted grids overlaid on a background (typically Cartesian) mesh. The separate generation of a body-fitted grid and a background grid allows great simplifications in the meshing process and at the same time allows modeling of complex systems with relative motion of parts of a structure, e.g., helicopter rotors (Pomin and Wagner, 2002). Previous attempts to carry out DNS using an unstructured (non-overlapping) mesh include the use of nested grids (Kravchenko et al., 1996), whereby the mesh spacing in each coordinate direction is made to increase with the wall distance. Issues associated with proper data exchange at the interface between zones with different spacing were pinpointed in that study, which reflected in imperfect statistics of velocity fluctuations.

The goal of this paper is to explore the capabilities of a novel Chimera algorithm to carry out high-fidelity numerical simulations of turbulent flow, including DNS, in an accurate and efficient fashion. The structure of the paper is the following: in section 2 we describe the numerical strategy, with particular emphasis on accurate and stable data exchange between the structured mesh and the underlying Cartesian mesh; in section 3, we present results of numerical tests to establish the formal accuracy of the method on simple benchmark problems, and then we apply it to the DNS of flow in a circular pipe in section 3.2. Finally, we utilize the described algorithm in the Detached Eddy simulation of the flow past a marine propeller in section 3.3, illustrating its applicability to engineering challenging problems. Concluding remarks wrap up the paper in section 4.

## 2 Numerical method

In this section, we outline the numerical algorithm, which is based on high-order central finite-difference discretization, with reference to block-structured grids with partial overlap. This approach is particularly well-suited for high-fidelity simulations of turbulent flow as it guarantees minimal, or even zero, numerical dissipation. First, we discuss high-order central schemes in curvilinear coordinate systems. We then provide details on evaluating the metric tensor in three-dimensional curvilinear grids, including extensions to Chimera grids. Additionally, we address the application of high-order numerical dissipation to control unphysical oscillations. In the latter part of the section, we explain grid topology computation, emphasizing techniques for cutting holes in the mesh and connecting different structured blocks.

### 2.1 Discrete model

We consider a set of curvilinear coordinates defined by the mapping  $x_k = x_k(\xi_j)$ , with  $j, k = 1, \dots, d$  ( $d$  is the number of spatial dimensions), where  $x_k$  expresses positions in the physical space, and  $\xi_j$  positions in the logical space. We start with the Euler equations of fluid dynamics cast in the strong conservation form (Vinokur, 1974),

$$\frac{\partial(J\mathbf{q})}{\partial t} + \frac{\partial}{\partial \xi_k} (J\xi_{k,j}\mathbf{f}_j) = 0, \quad (1)$$

with

$$\mathbf{q} = \begin{bmatrix} \rho \\ \rho u_i \\ \rho E \end{bmatrix}, \quad \mathbf{f}_j = \begin{bmatrix} \rho u_j \\ \rho u_i u_j + p \delta_{ij} \\ \rho u_j H \end{bmatrix}, \quad i = 1, \dots, d, \quad (2)$$

where  $\rho$  is the local fluid density,  $u_i$  denotes the Cartesian velocity component in the  $i$ -th direction,  $E = p/\rho/(\gamma - 1) + u_i u_i/2$ ,  $H = E + p/\rho$ , and  $J$  the determinant of the coordinate transformation. Here and throughout the paper the repeated index convention is used to indicate summation. For the present purposes we assume that the coordinate transformation is locally invertible and sufficiently smooth.

Pirozzoli (2011) showed that Eqn. (2) can be approximated with order of accuracy  $2L$  through centred formulas like

$$D_j \mathbf{f}_N = \sum_{\ell=1}^L a_\ell (\mathbf{f}_{j;\ell} - \mathbf{f}_{j;-\ell})_N, \quad (3)$$

where

$$(\mathbf{f}_{j;\ell})_N = \mathbf{f}_{\xi_1, \xi_2, \dots, \xi_{j+\ell}, \dots, \xi_d}. \quad (4)$$

Pirozzoli (2011) proved that several spitting of the convective terms yield numerical stability in curvilinear coordinates. In particular, he considered a locally conservative approximation of (2),

$$J \frac{d\mathbf{q}}{dt} + \sum_{j=1}^d \left( \frac{\mathbf{f}_{j,\ell} - \mathbf{f}_{j,-\ell}}{h_j} \right)_N = 0, \quad (5)$$

with numerical flux defined as

$$\mathbf{f}_{j,\ell} = 2 \sum_{\ell=1}^L a_\ell \sum_{m=1}^{\ell-1} \left[ \begin{array}{c} \widetilde{(\rho, \hat{u}_j, 1)}_{j;-m,\ell} \\ \widetilde{(\rho, \hat{u}_j, \mathbf{u})}_{j;-m,\ell} + (p, \widetilde{J\nabla \xi_j}, 1)_{j;-m,\ell} \\ \widetilde{(\rho, \hat{u}_j, H)}_{j;-m,\ell} \end{array} \right]_N, \quad (6)$$

where

$$\hat{u}_j = J \mathbf{u} \cdot \nabla \xi_j, \quad (7)$$

and the symbol  $\widetilde{(f, g, h)}_{j;-m,\ell}$  is the two-point, three-variable discrete averaging operator in the  $j$ th direction

$$\widetilde{(f, g, h)}_{j;-m,\ell} = \frac{1}{8} (f_{j;l} + f_{j;l-m}) (g_{j;l} + g_{j;l-m}) (h_{j;l} + h_{j;l-m}). \quad (8)$$

In Eqn. (5),  $h_j$  denotes the spacing along the  $j$ -th direction in the logical space. With no loss of generality, it is assumed to be unity throughout the rest of the paper.

In the formulas presented in this section, we frequently need to evaluate metric terms such as  $J\nabla \xi_j$ . The method for calculating the metric tensor with the desired level of accuracy, while maintaining a uniform flow on arbitrary overlapping meshes, is detailed in A and B.

## 2.2 High-order artificial dissipation

The approximation of equations (2) using central difference schemes and a co-located variable arrangement can result in odd-even decoupling of the numerical solution. This issue is exacerbated on Chimera grids due to the interpolation procedures at the boundaries, as discussed below.

To mitigate these high-frequency oscillations without compromising the formal accuracy of order  $2L$ , we introduce artificial dissipation terms. Assuming  $L \geq 2$ , we evaluate the divided differences recursively up to order  $2(L-1)$  in each spatial direction and for each scalar component of  $\mathbf{q}$ , such as  $u$ ,

$$\begin{cases} \Delta_i^1 u = u_i - u_{i-1}, & i = 2-L, \dots, N+L \\ \Delta_i^p u = \Delta_i^{p-1} u - \Delta_i^{p-1} u, & i = 1+p-L, N+L, \quad p = 2, \dots, 2L-2 \end{cases} \quad (9)$$

Then, for each variable  $u$ , at each interface  $i+1/2$ , we evaluate the oscillation indicator

$$\varphi_u|_{i+1/2} = \frac{\Delta_{i+L}^{(2L-2)} u}{(|\Delta_{i+L}^{(2L-3)} u| + |\Delta_{i+L-1}^{(2L-3)} u|)} \frac{\Delta_{i+L-1}^{(2L-2)} u}{(|\Delta_{i+L-1}^{(2L-3)} u| + |\Delta_{i+L-2}^{(2L-3)} u|)}. \quad (10)$$

Taking into account (9), inspection of equation (10) reveals that

$$-1 \leq \varphi_u|_{i+1/2} \leq 1, \quad (11)$$

and the extreme values are attained only when both conditions

$$\Delta_{i+L}^{(2L-3)} u \Delta_{i+L-1}^{(2L-3)} u < 0, \quad \text{and} \quad \Delta_{i+L-1}^{(2L-3)} u \Delta_{i+L-2}^{(2L-3)} u < 0, \quad (12)$$

hold, i.e. when a high-frequency oscillation on  $\Delta^{(2L-3)} u$  appears around the interface. Note that, when one of the condition in (12) holds, the corresponding ratio in (10) is equal to  $\pm 1$ . For instance, if the second condition holds, from the definition in (9), one has

$$\begin{aligned} \frac{\Delta_{i+L-1}^{(2L-2)} u}{(|\Delta_{i+L-1}^{(2L-3)} u| + |\Delta_{i+L-2}^{(2L-3)} u|)} &= \frac{\Delta_{i+L-1}^{(2L-3)} - \Delta_{i+L-2}^{(2L-3)}}{(|\Delta_{i+L-1}^{(2L-3)} u| + |\Delta_{i+L-2}^{(2L-3)} u|)} = \\ &= \pm \frac{(|\Delta_{i+L-1}^{(2L-3)} u| + |\Delta_{i+L-2}^{(2L-3)} u|)}{(|\Delta_{i+L-1}^{(2L-3)} u| + |\Delta_{i+L-2}^{(2L-3)} u|)} = \pm 1. \end{aligned}$$

Under this condition, Taylor series expansion shows that

$$\varphi_u|_{i+1/2} = \left[ \frac{u_\xi^{(2L-2)}}{2|u_\xi^{(2L-3)}|} \right]_{i+1} h + O(h^2) = \left[ \frac{u_\xi^{(2L-2)}}{2|u_\xi^{(2L-3)}|} \right]_{i+1/2} h + O(h^2), \quad (13)$$

where  $u^{(L')} = \partial^{L'} u / \partial \xi^{L'}$ . At all other interfaces

$$\begin{aligned} \varphi_u|_{i+1/2} &= \frac{[u_\xi^{(2L-2)}]_{i+1}}{2|u_\xi^{(2L-3)}|_{i+1}} \frac{[u_\xi^{(2L-2)}]_i}{2|u_\xi^{(2L-3)}|_i} h^2 + O(h^4) \\ &= \left[ \frac{u_\xi^{(2L-2)}}{2|u_\xi^{(2L-3)}|} \right]_{i+1/2}^2 h^2 + O(h^4). \end{aligned} \quad (14)$$

We then introduce the coefficient

$$\tilde{\varphi}|_{i+1/2} = \max(0, -\varphi|_{i+1/2}), \quad (15)$$



which is positive only where  $[u_\xi^{(2L-2)}]_{i+1} [u_\xi^{(2L-2)}]_i < 0$ , and which is unity only where both conditions in (12) hold; elsewhere, it is  $O(h)$ .

Finally, we determine the artificial dissipative flux at the interface  $i + 1/2$  for each variable as

$$\begin{aligned} f_u^a|_{i+1/2} &= \kappa \frac{(-1)^L}{2^{2L-1}} \lambda_{\max}|_{i+1/2} |J\nabla\xi|_{i+1/2} \tilde{\varphi}|_{i+1/2} (\Delta_{i+L}^{2L-2}u - \Delta_{i+L-1}^{2L-2}u) \\ &= \mathcal{A}_{i+1/2} \tilde{\varphi}|_{i+1/2} (\Delta_{i+L}^{2L-2}u - \Delta_{i+L-1}^{2L-2}u), \end{aligned} \quad (16)$$

where  $\kappa = O(1)$ ,  $\lambda_{\max}$  is the maximum eigenvalue of the Jacobian matrix of  $\mathbf{f}_{j;\ell}$ , namely

$$\lambda_{\max}|_{i+1/2} = \max(\lambda_{\max}|_i, \lambda_{\max}|_{i+1}), \quad (17)$$

and finally

$$\mathcal{A}_{i+1/2} = \kappa \frac{(-1)^L}{2^{2L-1}} \lambda_{\max}|_{i+1/2} |J\nabla\xi|_{i+1/2}. \quad (18)$$

Taylor series expansion proves that

$$\begin{aligned} f_u^a|_{i+1/2} &= \mathcal{A}_{i+1/2} \left[ \left( \frac{u_\xi^{(2L-2)}}{2|u_\xi^{(2L-3)}|} \right)^\sigma u_\xi^{(2L-1)} h^{2L-1} \right]_{i+1/2} + O(h^{2L+\sigma}) \\ &= \mathcal{A}_{i+1/2} \left[ \left( \frac{u_\xi^{(2L-2)}}{2|u_\xi^{(2L-3)}|} \right)^\sigma u_\xi^{(2L-1)} \right]_{i+1/2} h^{2L+\sigma-1} + O(h^{2L+\sigma}), \end{aligned} \quad (19)$$

where  $\sigma = 0, 1$  or  $2$ . Note that  $\sigma = 0$  only at the interfaces where the sign of the order  $2L - 2$  derivative changes, in which case  $f_u^a = O(h^{2L-1})$ . At all the other points  $f_u^a = O(h^{2L})$  at least (it is exactly zero at interfaces where  $[u_\xi^{(2L-2)}]_{i+1} [u_\xi^{(2L-2)}]_i > 0$ ), and therefore the formal order of accuracy of the original central scheme is retained.

Linear stability analysis and numerical tests convey that the time step restriction due to this form of artificial dissipation is

$$\Delta t \leq \min_{i, \tilde{\varphi} > 0} \frac{C}{\kappa \left( [\tilde{\varphi} |\nabla\xi| \lambda_{\max}]_{i-1/2} + [\tilde{\varphi} |\nabla\xi| \lambda_{\max}]_{i+1/2} \right)}, \quad (20)$$

where  $C = O(1)$  depends on the time integration scheme. For all the test cases herein reported, we have used  $\kappa = 0.1$ ; hence, the incurred time step constraint is very mild. When second-order discretization is used ( $L = 1$ ), we use the same artificial dissipation as for  $L = 2$

### 2.3 Grid topology

In the following, we assume that the mesh consists of blocks  $\mathcal{B}_b$ ,  $b = 1, 2, \dots, N_B$ , each with structured ordering and including  $n_i^b \times n_j^b \times n_k^b$  points in directions  $i, j$  and  $k$ , respectively. The blocks can have partial overlap. The computation of the flow on Chimera grids requires the knowledge of active cells and holes in every block, together with block-to-block connection to interpolate the solution where needed. The rationale for identifying active cells and holes in the grid is the most obvious, as we want to retain the best discretization available at each point. For this purpose, we must check each cell to verify whether

1. there is another cell overlapping with the candidate cell;

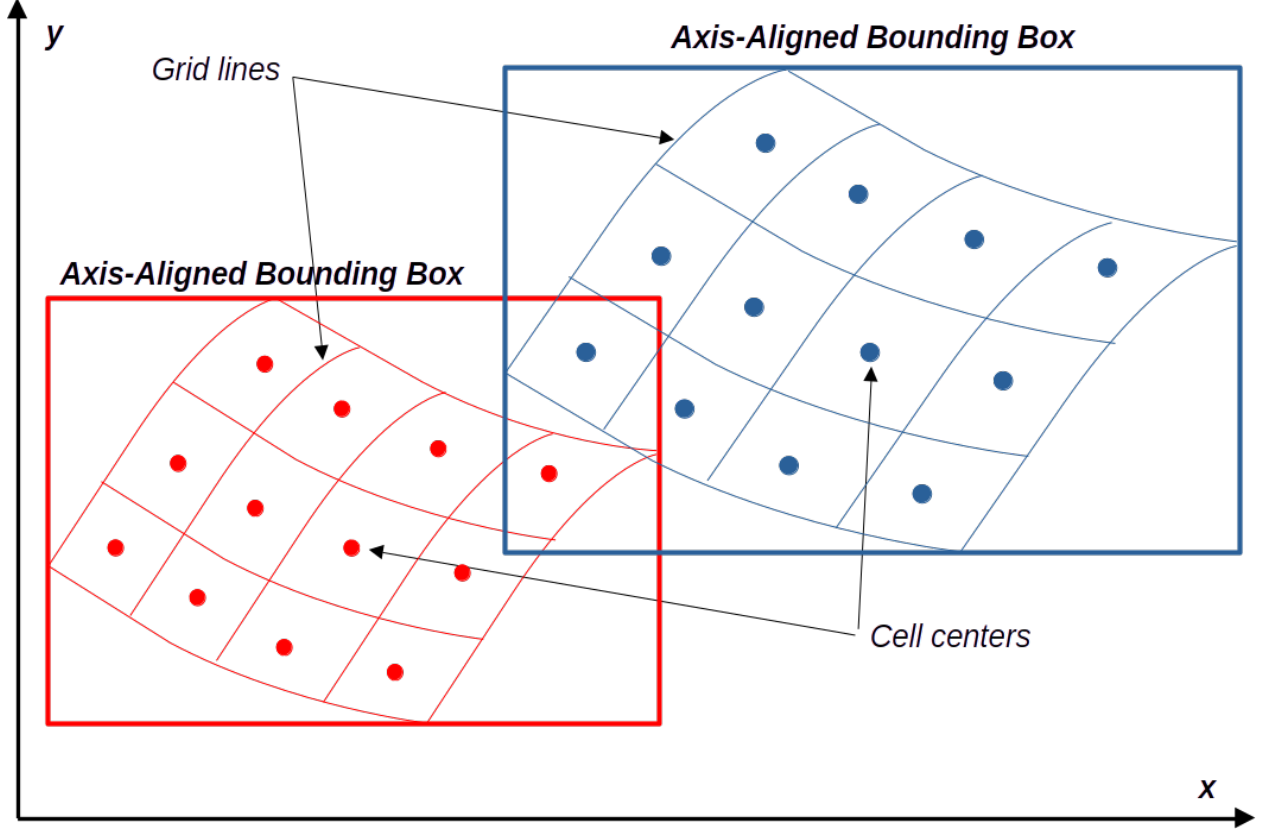


Figure 1: Sketch of grid lines, cell centres and bounding boxes

2. the overlapping cell is "smaller" in the sense specified in the following.

A similar criterion guides the selection of donors for the interpolation of the solution among blocks at interior points and at those block interfaces that are neither natural boundaries (e.g. walls, symmetry planes, inflow, outflow) nor matching faces between blocks (i.e. where there is an actual continuity in the grid). In both cases, we may find more than one possible donor. In this situation, we choose the donor whose size is closest to the cell under analysis. As for the definition of the cell size ( $d$ ), one can adopt either  $d = \sqrt[3]{V}$  ( $V$  being the cell volume) or the cell diagonal  $d = d_c$ . When dealing with high-Reynolds-number flows with highly stretched grids, in order to retain all the cells close to solid walls, we define the cell dimension as

$$d = \min(d_n, d_c) \quad \text{or} \quad d = \min(d_n, \sqrt[3]{V}), \quad (21)$$

where  $d_n$  is the distance from the wall. With this definition,  $d \rightarrow 0$  near the walls, and no other cell can cancel those in the boundary layers.

## 2.4 Search algorithm for donors

The computation of grid topology must be efficient to avoid negatively impacting the overall CPU time, particularly in problems involving moving boundaries (Di Mascio et al., 2022), where the grid topology must be updated at each time step. To accelerate the process of hole identification and donor computation, we draw inspiration from the classical Overlapped Cartesian Grid procedure

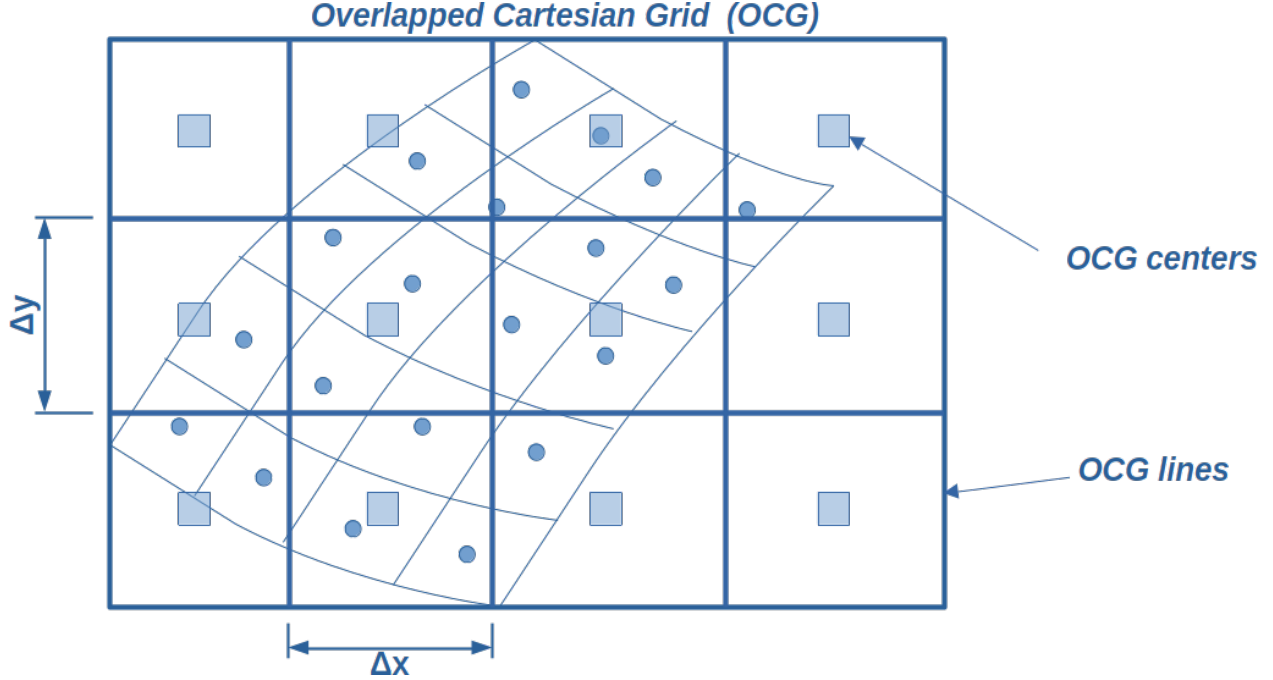


Figure 2: Sketch of overlapping Cartesian grid

developed by Verlet (1967), widely used in particle methods. This approach has been adapted to work effectively with block-structured meshes that allow for partial overlap. The first step involves constructing an Axis-Aligned Bounding Box (AABB) for each block  $\mathcal{B}_b$ . This box is defined as the smallest axis-aligned parallelepiped that contains all the points within the block. This method ensures computational efficiency while maintaining compatibility with the block-structured grid framework. This bounding box is such that

$$\begin{cases} x_{\min}^{BB} \leq x_{i,j,k} \leq x_{\max}^{BB} \\ y_{\min}^{BB} \leq y_{i,j,k} \leq y_{\max}^{BB} \\ z_{\min}^{BB} \leq z_{i,j,k} \leq z_{\max}^{BB} \end{cases} \quad \forall (i,j,k) \in \mathcal{B}_b, \quad (22)$$

Therefore, entire blocks can be excluded from the search for donors as one of the following six conditions is satisfied for the generic cell centre  $(\vec{x}_c)$ :

$$\begin{aligned} x_c &< x_{\min}^{BB}, & x_c &> x_{\max}^{BB}, \\ y_c &< y_{\min}^{BB}, & y_c &> y_{\max}^{BB}, \\ z_c &< z_{\min}^{BB}, & z_c &> z_{\max}^{BB}. \end{aligned} \quad (23)$$

Moreover, possible holes in block  $p$  must search for possible donors in block  $q$  only when there is a partial overlap between the corresponding bounding boxes, as sketched in figure 1 for a two-dimensional problem.

Once the AABB for each block is identified, it is partitioned into a Cartesian grid with uniform spacing in each direction, as illustrated in Figure 2. Generally, the grid spacing satisfies  $\Delta x \neq \Delta y$ . The number of points in the Overlapped Cartesian Grid (OCG) is typically much smaller than

the number of points in the underlying curvilinear mesh. For example, the number of points in each direction of the OCG is often  $n_i^{OCG} = O(n_i^b/4)$  to  $O(n_i^b/8)$ . As a result, the total number of cells in the OCG is reduced to approximately  $O(n_i \times n_j \times n_k/64)$  to  $O(n_i \times n_j \times n_k/512)$ . This significant reduction ensures minimal overhead in computer memory usage. In each cell of the OCG, we store the index of the closest point in the underlying grid and flag the empty cells. To achieve this, all OCG cells are initially initialized with an invalid index (e.g., a negative value if grid numbering starts from zero or one) and a large value for the current distance (e.g.,  $10^{10}$  if the typical distance is  $O(1)$ ). Next, we visit all cell centers of the underlying curvilinear mesh, determining the corresponding indices of the OCG cell where they belong,

$$\begin{aligned} i_{OCG} &= \left\lfloor \frac{x_{i,j,k} - x_{\min}^{BB}}{\Delta x} \right\rfloor + 1, \\ j_{OCG} &= \left\lfloor \frac{y_{i,j,k} - y_{\min}^{BB}}{\Delta y} \right\rfloor + 1, \\ k_{OCG} &= \left\lfloor \frac{z_{i,j,k} - z_{\min}^{BB}}{\Delta z} \right\rfloor + 1, \end{aligned} \quad (24)$$

where  $\lfloor \cdot \rfloor$  denotes the integer part and the numbering of the OCG starts from one. We then store the index of the cell centres if the distance is smaller than the last saved value. An invalid index remains in the OCG cells not visited in the loop.

The OCG thus identified is useful for quick search of possible donors with the procedure described in the pseudo-code 1.

## 2.5 Local search algorithm

Next, we search for the closest cell center using the information stored in the OCG, progressing along each curvilinear coordinate line. Figure 3 illustrates the local search algorithm for a two-dimensional problem, with the three-dimensional case following an analogous logic. The search begins at point  $\vec{x}_{p_0}$  in the figure. In each direction, we evaluate the distance (specifically, the squared distance to save CPU time) from the candidate hole to the two adjacent points and move towards the closer one. For example, when moving along the  $\xi$  coordinate line in Figure 3, we find that point  $\vec{x}_\xi$  is the closest to  $\vec{x}_h$  along that line. Next, we proceed along the other direction (denoted as  $\eta$  in the example) and repeat the procedure until we reach point  $\vec{x}_\eta$ , which is the closest to  $\vec{x}_h$  along the  $\eta$  direction. The search alternates between the  $\xi$  and  $\eta$  directions until it converges at the point with the minimum distance, completing the process.

This simple search algorithm is efficient but can sometimes identify an incorrect cell center as the candidate donor. This issue is illustrated in the top panel of Figure 4: point **A** is the closest cell center of the block, but it does not lie within the corresponding cell. This problem arises when the grid lacks high regularity. To address this limitation for general grids, we refine the search by checking a distance metric based on the covariant components of the position vectors after initially identifying the closest point using the original algorithm. Specifically, any position vector can be expressed as

$$\vec{y} = \tilde{y}^i \vec{e}_i, \quad \text{where} \quad J\tilde{y}^i = \vec{y} \cdot \vec{e}^i, \quad (25)$$

with  $\vec{e}_i = \partial \vec{x} / \partial \xi_i$ ,  $\vec{e}^i = J \nabla \xi_i$ , and  $J$  representing the covariant vectors, contravariant vectors, and the Jacobian of the coordinate transformation  $\vec{x}(\xi_k)$ , respectively. Using this formulation, we define the effective distance between two points,  $\vec{y}_A$  and  $\vec{y}_C$ , as:

$$\tilde{d}^2 = [\tilde{y}_A^i - \tilde{y}_C^i]^2. \quad (26)$$

---

**Algorithm 1** Donor search - pseudocode

---

```
for all  $\mathcal{B}_b \in \mathcal{M}$  do                                 $\triangleright$  (Mesh  $\mathcal{M}$  made of blocks  $\mathcal{B}_b$ ,  $b = 1, 2, \dots, N_B$ )  
  
  for all  $\vec{x}_c \in \mathcal{B}_b$  do  
     $\mathbf{C}_c = \text{cell around } \vec{x}_c$   
     $d_c = \text{dimension of } \mathbf{C}_c$   
  
    for all  $\mathcal{B}_p$ ;  $p \neq b$  do  
  
      if  $\vec{x}_c \in \mathcal{AABB}_p$  then                                 $\triangleright$  ( $\mathcal{AABB}_p$  is the AABB for block  $p$ )  
        Find  $\mathcal{OCG}_p$  cell                                 $\triangleright$  ( $\mathcal{OCG}_p$  is the OCG for block  $p$ )  
         $p_0 : \text{index saved in the } \mathcal{OCG}_p \text{ cell}$   
  
        if  $p_0$  is a valid index then  
  
          Start from  $\vec{x}_{p_0}$   
          Find the closest cell center  $\vec{x}_p$  (see subsection 2.5)  
           $\mathbf{C}_p = \text{cell around } \vec{x}_p$   
  
          if  $\vec{x}_c \in \mathbf{C}_p$  then  
             $d_p = \text{dimension of } \mathbf{C}_p$   
            if  $d_p < d_c$  then  
               $\mathbf{C}_c \rightarrow \text{Hole}$   
              if Already found a donor then  
                 $\mathbf{C}_{\text{previous}} = \text{old donor cell}$   
                 $d_{\text{previous}} = \text{dimension of } \mathbf{C}_{\text{previous}}$   
                if  $|d_p - d_c| < |d_{\text{previous}} - d_c|$  then  
                   $\mathbf{C}_p \rightarrow \text{Donor}$   
              else  
                 $\mathbf{C}_p \rightarrow \text{Donor}$ 
```

---

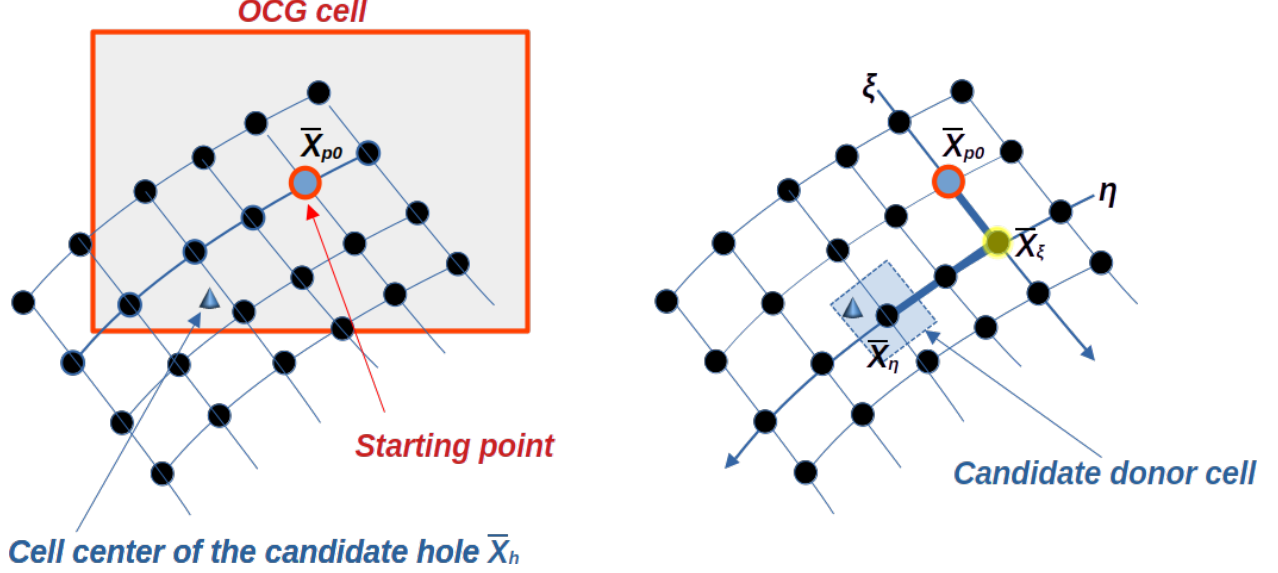


Figure 3: Sketch of the search algorithm

Graphically, as shown in the middle panel of Figure 4, this distance is the sum of the squared lengths of the two segments indicated by thick blue dashed lines. By employing this definition of distance, the refined search algorithm correctly identifies point **B** as the cell center containing  $\vec{x}_h$ , resolving the issue encountered with point **A**.

Once the candidate donor cell is identified, we accept it as a donor if it meets the criteria outlined in the previous section. Finally, we interpolate the solution from the active donor cells to the hole cells. We have implemented two levels of interpolation accuracy:

- *second-order accurate interpolation*: In this method, we select a convex set of four cell centers in 2D (or eight in 3D), which includes the identified donor cell, surrounding the center of the hole. The solution is transferred from the donor and surrounding cells using bilinear interpolation in 2D (or trilinear in 3D). This process is illustrated in the bottom panel of Figure 4.
- *fourth-order accurate interpolation*: For higher accuracy, we select a convex set of sixteen cell centers in 2D (or sixty-four in 3D), which also includes the identified donor cell, around the hole center. The solution is transferred from the donor and surrounding cells using the Cartesian product of two cubic interpolation functions in 2D (or three cubic functions in 3D). The set of points used for interpolation is defined by adding an additional layer of donor cells on each side of the set used for second-order interpolation.

These approaches ensure accurate solution transfer while accommodating varying accuracy requirements.

## 2.6 Forcing terms for the governing equations

Once the grid topology is determined, we do not remove the holes from the discrete model. Instead, we employ a technique adapted from the immersed-boundary method community (Verzicco, 2023). Specifically, we introduce a forcing term into the discretized equations at the hole locations, as

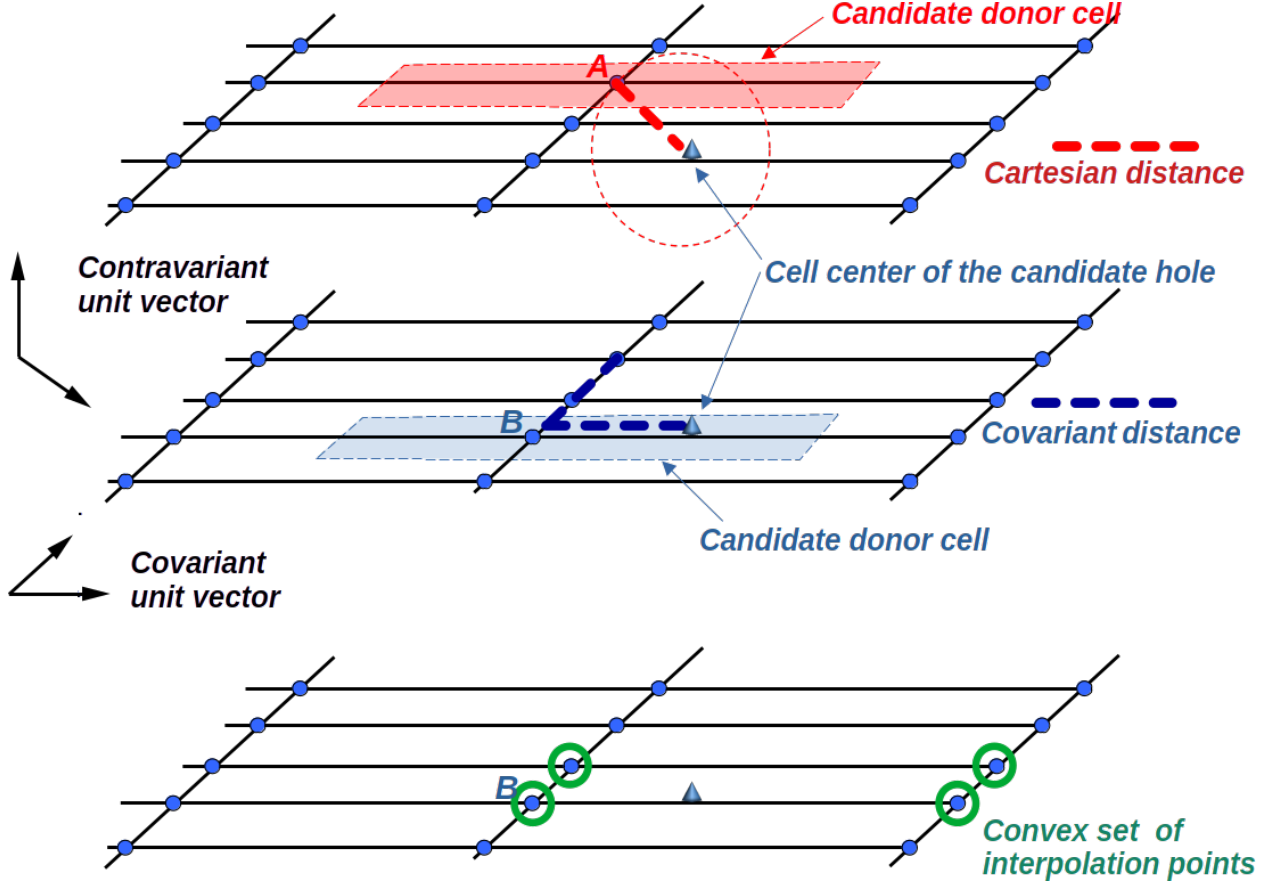


Figure 4: Sketch of the search algorithm - Local search

follows:

$$\frac{d\mathbf{q}_n}{dt} + \mathcal{L}_n^h(\mathbf{q}_{n-p}, \mathbf{q}_{n+q}) + \frac{K}{\delta_n}(\mathbf{q}_n - \hat{\mathbf{q}}_n) = 0 \quad n = 1, \dots, N$$

where  $\mathbf{q}_n$  is the state variable vector at point  $n$ ,  $\mathcal{L}_n^h$  is the discrete operator at the same point,  $p$  and  $q$  are parameters depending on the discrete model, and  $\hat{\mathbf{q}}_n$  is the interpolated state vector at point  $n$ . Furthermore,  $K$  is a constant of order  $O(1) \div O(10)$ , and  $\delta_n$  has the physical dimension of time, defined as:

$$\delta_n = \min \left( \Delta t, \frac{\Delta \xi}{\lambda_\xi}, \frac{\Delta \eta}{\lambda_\eta}, \frac{\Delta \zeta}{\lambda_\zeta} \right),$$

where  $\Delta t$  is the time step, and  $\Delta \xi, \Delta \eta, \Delta \zeta$  are the grid step sizes in the coordinate directions  $\xi, \eta, \zeta$ , respectively. The values  $\lambda_\xi, \lambda_\eta, \lambda_\zeta$  represent the spectral radii of the Jacobian matrices of the fluxes in each direction. Several motivations suggest the use of this procedure:

1. the data structure remains identical to traditional block-structured grids;
2. all the algorithms developed for block-structured grids (e.g. geometrical multi-grid, alternate directions method, incomplete LU factorization) remain identical; hence, we can use existing software for structured blocks;
3. when dealing with moving grids, we already have the values at re-activated cells without any additional coding;

4. the last term in equation (2.6) causes exponential relaxation of the solution towards the interpolated value  $\hat{\mathbf{q}}_n$  with time constant  $\delta$ : this term contributes to damping possible spurious waves forming between blocks with large differences in grid size.

### 3 Results

#### 3.1 Advection of homentropic vortex

As an initial test, we considered the passive advection of a circular, homentropic, zero-circulation vortex, a benchmark case studied by many researchers. The initial velocity, density, and pressure are specified as follows:

$$\begin{aligned}\frac{u(x, y)}{u_\infty} &= 1 - \frac{M_v}{M_\infty} \frac{y - y_0}{r_v} e^{(1-\hat{r}^2)/2}, \\ \frac{v(x, y)}{u_\infty} &= \frac{M_v}{M_\infty} \frac{x - x_0}{r_v} e^{(1-\hat{r}^2)/2}, \\ \frac{\rho(x, y)}{\rho_\infty} &= \left(1 - \frac{\gamma - 1}{2} M_v^2 e^{1-\hat{r}^2}\right)^{\frac{1}{\gamma-1}}, \\ \frac{p(x, y)}{p_\infty} &= \left(1 - \frac{\gamma - 1}{2} M_v^2 e^{1-\hat{r}^2}\right)^{\frac{\gamma}{\gamma-1}},\end{aligned}$$

where  $(x_0, y_0)$  are the initial coordinates of the vortex center,  $r_v$  is the radius of the vortex core,  $M_v$  is the vortex Mach number (based on the maximum vortex-induced tangential velocity),  $M_\infty$  is the free-stream Mach number,  $\hat{r} = r/r_v$ , and  $r^2 = (x - x_0)^2 + (y - y_0)^2$ . In our tests, we considered  $M_v = 0.1$  and  $M_\infty = 0.1$ . This test case is helpful because it has an analytical solution, as the vortex is passively advected when the physical viscosity is zero. The results of the numerical experiments are presented below for both a block-structured Cartesian grid with overlap and a block-structured curvilinear grid with overlap.

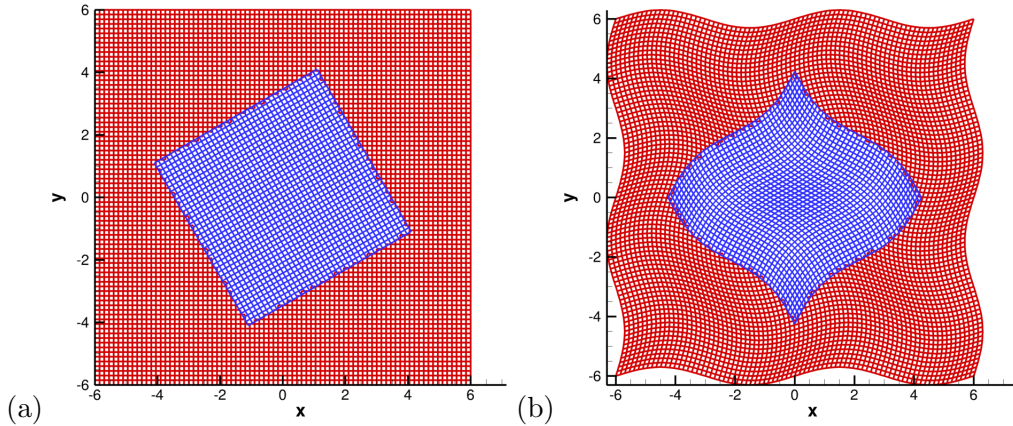


Figure 5: Cartesian overlapping meshes (a) and curvilinear overlapping meshes (b) for the homentropic vortex advection test case. In both cases, the background mesh (red) includes  $80 \times 80$  grid points, and the internal mesh (blue) includes  $40 \times 40$  grid points.

The two meshes are shown in Figure 5. In the illustration, the background mesh consists of  $80 \times 80$  grid points, while the internal mesh contains  $40 \times 40$  grid points. For Cartesian meshes (panel (a)), the internal mesh is rotated by  $30^\circ$  relative to the background. For curvilinear meshes (panel (b)),



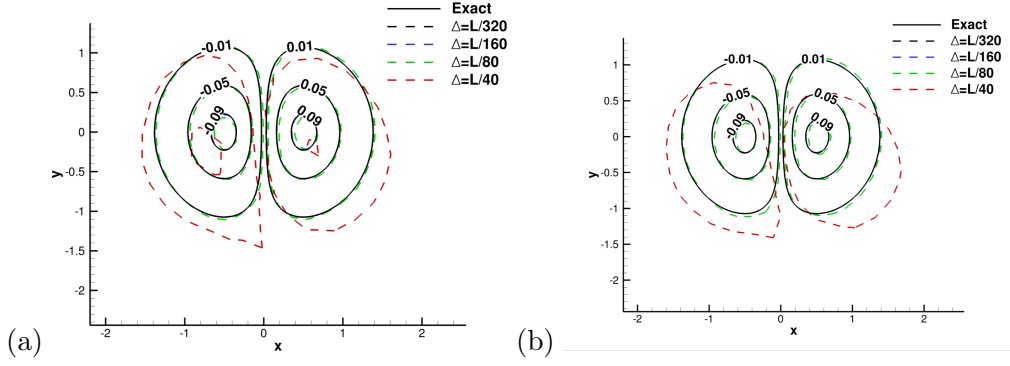


Figure 6: Homentropic vortex advection: comparison of computed vertical velocity contours with the exact solution (solid line), after one flow-through time. Results are shown for the Cartesian overlapping mesh (a) and the curvilinear overlapping mesh (b).

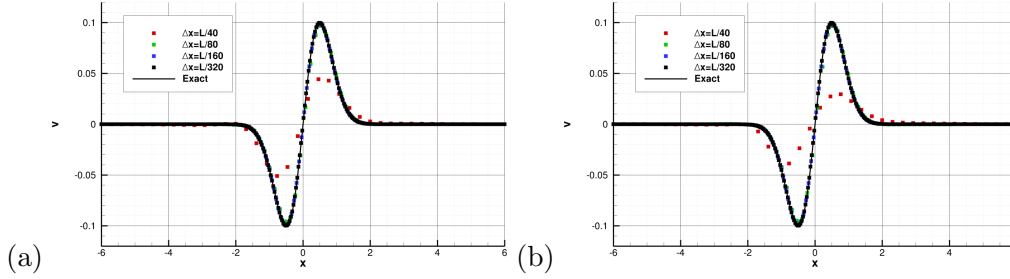


Figure 7: Homentropic vortex advection: comparison of computed vertical velocity profiles with the exact solution (solid line), after one flow-through time. Results are shown for the Cartesian overlapping mesh (a) and the curvilinear overlapping mesh (b).

both the external and internal meshes are smoothly distorted. In both cases, periodic boundary conditions are applied to the background mesh, which provides boundary conditions for the internal meshes through the Chimera interpolation described earlier. The numerical simulations reported here employ fourth-order accurate central discretization and fourth-order Chimera interpolation across non-conforming mesh boundaries. We used the classical fourth-order Runge-Kutta scheme for time integration.

Figure 6 presents the computed vertical velocity contours after one flow-through time, comparing them with the exact solution (solid black lines). On the coarsest Cartesian mesh, with a resolution of  $L/\Delta = 40$ , the vortex exhibits significant deformation. This distortion is even more pronounced on the curvilinear mesh at the same resolution, as expected. However, deviations from the exact solution are negligible on the next finer mesh, with a resolution of  $L/\Delta = 80$ , for both Cartesian and curvilinear grids.

A more detailed view is provided in Figure 7, which shows velocity profiles across the vortex. The results confirm that the coarsest mesh, which resolves the vortex radius with only about six points, is inadequate for accurately representing the vortex structure. This inadequacy leads to underestimation of the maximum velocity and introduces oscillatory behavior in the velocity profile. In contrast, finer grids exhibit significantly smaller deviations from the analytical solution, demonstrating clear grid convergence with mesh refinement.

Figure 8 also quantifies grid convergence by plotting the  $L_2$  error norm for the vertical velocity as a function of grid resolution. The results confirm that the solver retains full nominal fourth-

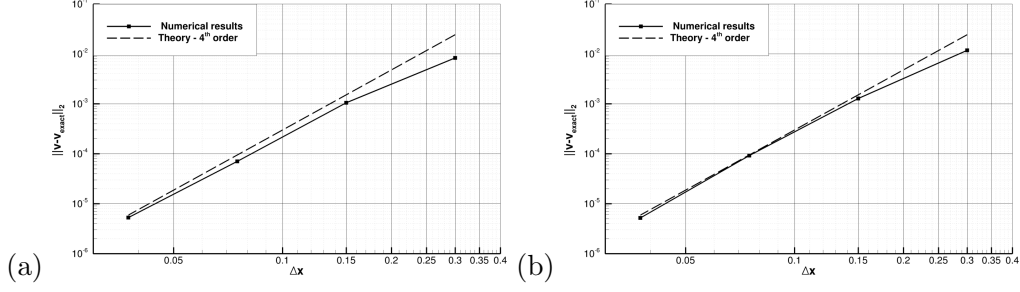


Figure 8: Homentropic vortex advection:  $L_2$  error norm on vertical velocity as a function of grid resolution, for the Cartesian overlapping mesh (a) and the curvilinear overlapping mesh (b).

order accuracy, even in the presence of non-conforming boundaries, through the use of fourth-order block-to-block interpolation. Use of curvilinear meshes in this case only yields marginally higher absolute error, but nevertheless the asymptotic convergence rate is maintained.

### 3.2 DNS of turbulent pipe flow

In this section, we analyze pressure-driven turbulent flow in a circular pipe, a configuration first investigated using DNS by Eggels et al. (1994). This flow is considered one of the most canonical cases of wall-bounded turbulence, with extensive reference data from both experimental and numerical studies. The computational setup adopted here is identical to that of Pirozzoli et al. (2021). Specifically, the simulations are performed by imposing a constant axial forcing term to mimic the effect of a driving pressure gradient. Periodic boundary conditions are applied along the axial direction, assuming fully developed flow, with the pipe length set to fifteen times its radius.

Unlike the previous test case, the present computation uses an incompressible flow model with viscosity. The viscous terms are approximated with a second-order centered scheme, and the time derivatives are discretized using a standard three-point backward, fully implicit formula. As a result, the global accuracy of the scheme is second-order. Since the resulting system of algebraic equations is fully implicit, it is solved using a multi-grid technique and dual time stepping (see, e.g., Di Mascio et al., 2014; Muscari et al., 2017; Magionesi et al., 2018; Di Mascio et al., 2022). To validate the numerical methodology, we simulate a flow at a low Reynolds number ( $Re_b = 5300$ ), consistent with the study by Eggels et al. (1994). Our results are compared with DNS data obtained in a cylindrical coordinate system (Pirozzoli et al., 2021), which serve as a reference.

This study employed two mesh configurations, as illustrated in figure 9. The first configuration consists of a block-structured mesh comprising one inner and four outer blocks arranged in an abutting setup without overlap. Each outer block contains  $64 \times 32 \times 256$  points in the peripheral, radial, and streamwise directions, respectively, while the inner block contains  $65 \times 65 \times 256$  points, resulting in a total of 3.15 million points. The second configuration utilizes a curvilinear polar mesh for the outer region of the pipe, comprising  $256 \times 48 \times 256$  points in the peripheral, radial, and streamwise directions, respectively. A Cartesian mesh is used for the pipe core, consisting of  $33 \times 33 \times 256$  points, bringing the total to 3.4 million points. The Chimera interpolation algorithm is employed to manage the overlap between the polar and Cartesian regions. For both mesh configurations, the grid points are clustered toward the solid boundary, ensuring that the wall-normal thickness satisfies  $d^+ = du_\tau/\nu < 1$ , where  $u_\tau$  is the friction velocity. The non-dimensional time step is set to  $1 \times 10^{-3}$ , guaranteeing a CFL number not exceeding 0.5. The numerical simulations were advanced in time until the pressure gradient achieved statistical convergence. Afterwards, they were continued for approximately one hundred flow-through times to ensure robust statistical

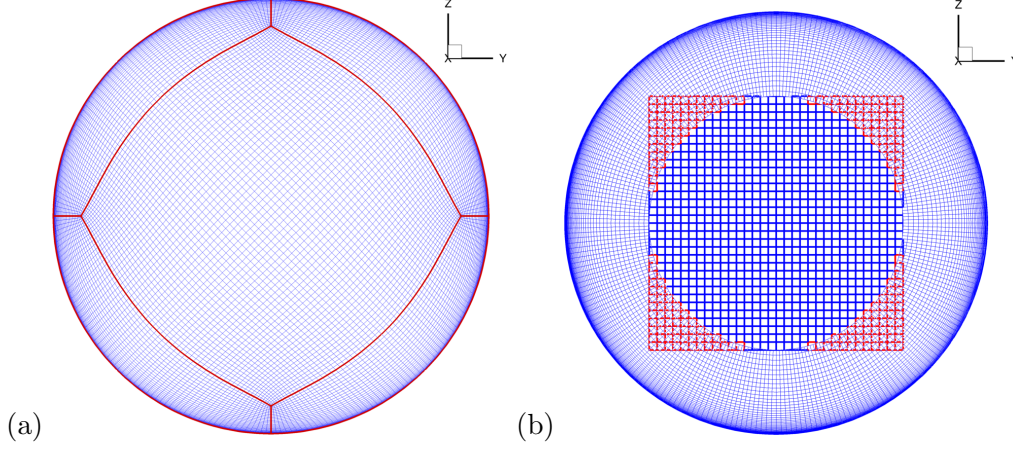


Figure 9: Computational meshes for DNS of turbulent pipe flow: (a) block-structured mesh (edges in red); and (b) overlapping (Chimera) mesh (blanked cells in red).

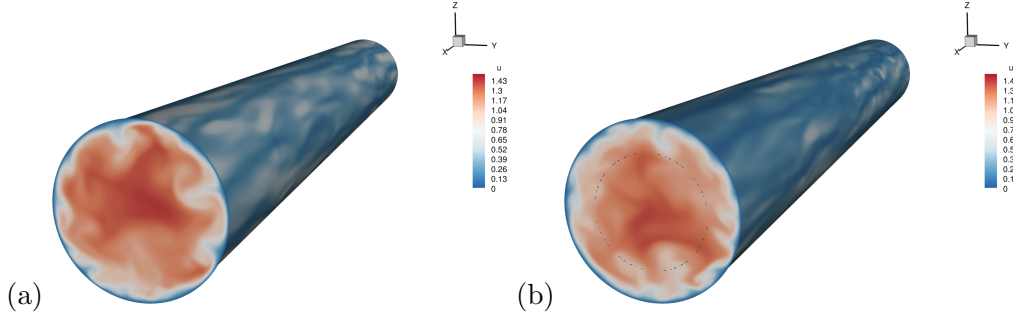


Figure 10: DNS of turbulent pipe flow: instantaneous streamwise velocity fields obtained with a block-structured mesh (a) and a Chimera mesh (b).

sampling.

Figure 10 shows instantaneous axial velocity contours in both a cross-stream plane and a near-wall plane. The flow exhibits the characteristic features of pipe turbulence, including near-wall streaks with alternating regions of high- and low-speed momentum (depicted in red and blue, respectively). The cross-stream plane highlights large-scale sweeps and ejections, which play a critical role in momentum exchange. Notably, while the velocity fields are nominally sampled at the same time instants, discrepancies arise due to the sensitive dependence of instantaneous turbulent flow realizations on initial conditions and mesh geometry.

Figure 11 displays iso-lines of the streamwise velocity. The cross-stream slices reveal that the axial velocity is perfectly smooth in the case of the abutting mesh (panel a). Similarly, excellent continuity is achieved with the Chimera mesh (panel b). Notably, in the overlapping region between the outer mesh (solid lines) and the inner mesh (dashed lines), the velocity contours align closely, demonstrating the effectiveness and accuracy of the interpolation procedure. Further validation is provided in panel (c), which shows a longitudinal slice of the pipe for the Chimera mesh. As with the previous results, no visible discontinuities or numerical artifacts, such as wiggles, are observed across the transition region between the inner and outer meshes.

Figure 12 provides a quantitative evaluation of the flow statistics, presenting the mean velocity and velocity variance profiles obtained from DNS on both abutting and Chimera meshes. These results are compared with DNS data computed in cylindrical coordinates (Pirozzoli, 2024). The

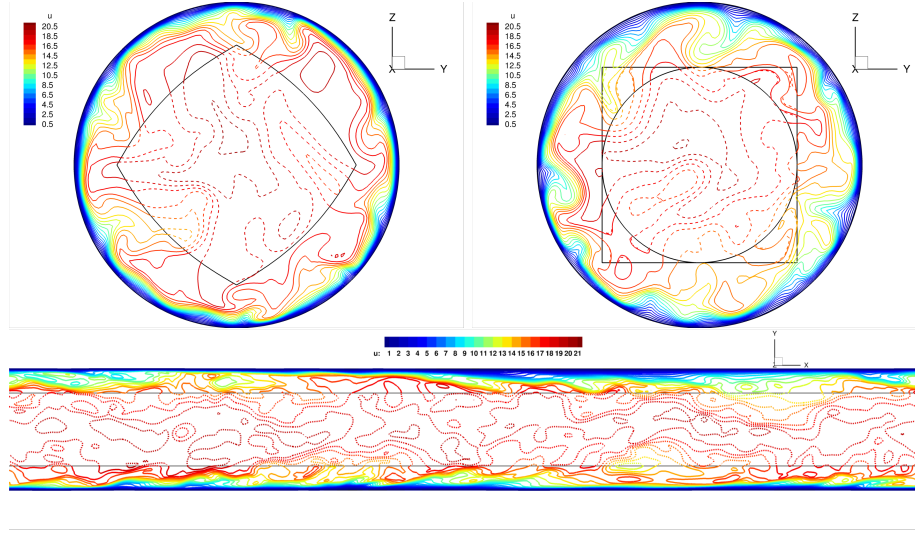


Figure 11: DNS of turbulent pipe flow: instantaneous streamwise velocity fields in a cross-stream plane obtained with a block-structured mesh (a) and a Chimera mesh (b); and longitudinal slice of instantaneous velocity field obtained with a Chimera mesh (c). Solid lines indicate velocity contours in the outer mesh, and dashed lines indicate velocity contours in the inner mesh.

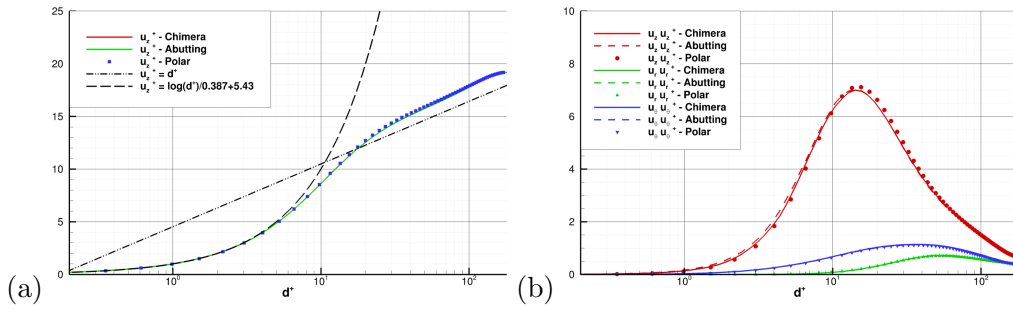


Figure 12: DNS of turbulent pipe flow: comparison of mean velocity profiles (a), and velocity variances, for the case of cylindrical coordinates (symbols Pirozzoli, 2024), abutting mesh (green) and Chimera mesh (red).

profiles show excellent agreement across all statistics, with no signs of localized spurious increases or reductions in the intensity of turbulent fluctuations.

As an additional verification, figure 13 presents iso-lines of the vorticity components, providing insight into potential errors in capturing small-scale turbulence across meshes with different resolutions. Vorticity, which involves derivatives of the velocity components, is a key metric for assessing the strength of turbulence at small scales (Moin and Kim, 1985). Once again, no evidence of discontinuities or numerical artifacts, such as jumps or wiggles, is observed near the mesh interfaces. Notably, the strong shear layers originating from the pipe wall are accurately transmitted into the interior mesh. Furthermore, the vorticity contours in the overlap region between the two meshes (depicted with solid and dashed lines) show excellent conformity, demonstrating the robustness and accuracy of the interpolation algorithm.

### 3.3 High-fidelity simulation of ship propeller wake

As a final example of application to actual engineering problems, we performed the computation of the flow past an isolated rotating propeller in mild loading conditions, for which both experimental data Felli et al. (2011) and numerical simulation are available Muscari et al. (2013). Figure 14 reports the geometry of the stock propeller INSEAN E779A, the surface grid, and two sections of the volume grid on the planes  $x = 0$  and  $z = 0$ . The complete grid consists of 501 partially overlapping blocks, for a total of approximately 21 million points.

We performed the computation in the rotating reference frame as a Detached Eddy Simulation (DES) Spalart et al. (1997) for a loading condition given by  $J = U_\infty/(nD) = 0.71$ , where  $J$  is the advance ratio,  $U_\infty$  is the speed of the undisturbed flow,  $n$  is the number of propeller revolutions per second, and  $D$  is the propeller diameter.

To evaluate numerical uncertainty, we carried out simulations at two grid levels. Specifically, the coarser grid was generated by removing every other grid point from the finer grid in each direction. The table on the left of Figure 15 compares the computed thrust and torque coefficients on both grid levels with the experimental measurements. The right part of the figure compares the computed tip vortices, shown in red and visualized as suggested by Jeong and Hussain (1995), with the experimental tip vortices, visualized by inducing vortex core cavitation. The agreement between numerical and experimental data is very satisfactory regarding both force coefficients and wake topology.

Finally, Figure 16 presents the solution in terms of tip vortices, identified as suggested in Jeong and Hussain (1995) with  $\lambda_2 = -1$ , along with the vorticity field on the plane  $z = 0$ . The bottom part of the figure shows the axial velocity and pressure fields. The figure clearly demonstrates that the tip vortex can persist while gradually thickening over a long distance downstream of the propeller, due to the near absence of numerical dissipation. This behavior would not be possible with conventional, non-energy-conserving algorithms. We would like to particularly emphasize that, as with the flow in the circular pipe, the solution develops smoothly without discontinuities across the overlapping blocks, even in the far field where the grid is coarsened to save CPU time.

## 4 Conclusions

We have presented a computational framework for high-fidelity simulations of turbulent flows based on the Chimera approach. This methodology employs multiple overset meshes, potentially with varying resolutions and/or coordinate systems, to model complex geometries and flow phenomena effectively. These meshes can either move relative to one another or remain static. The proposed computational approach utilizes a central discretization applied to the split form of the convective

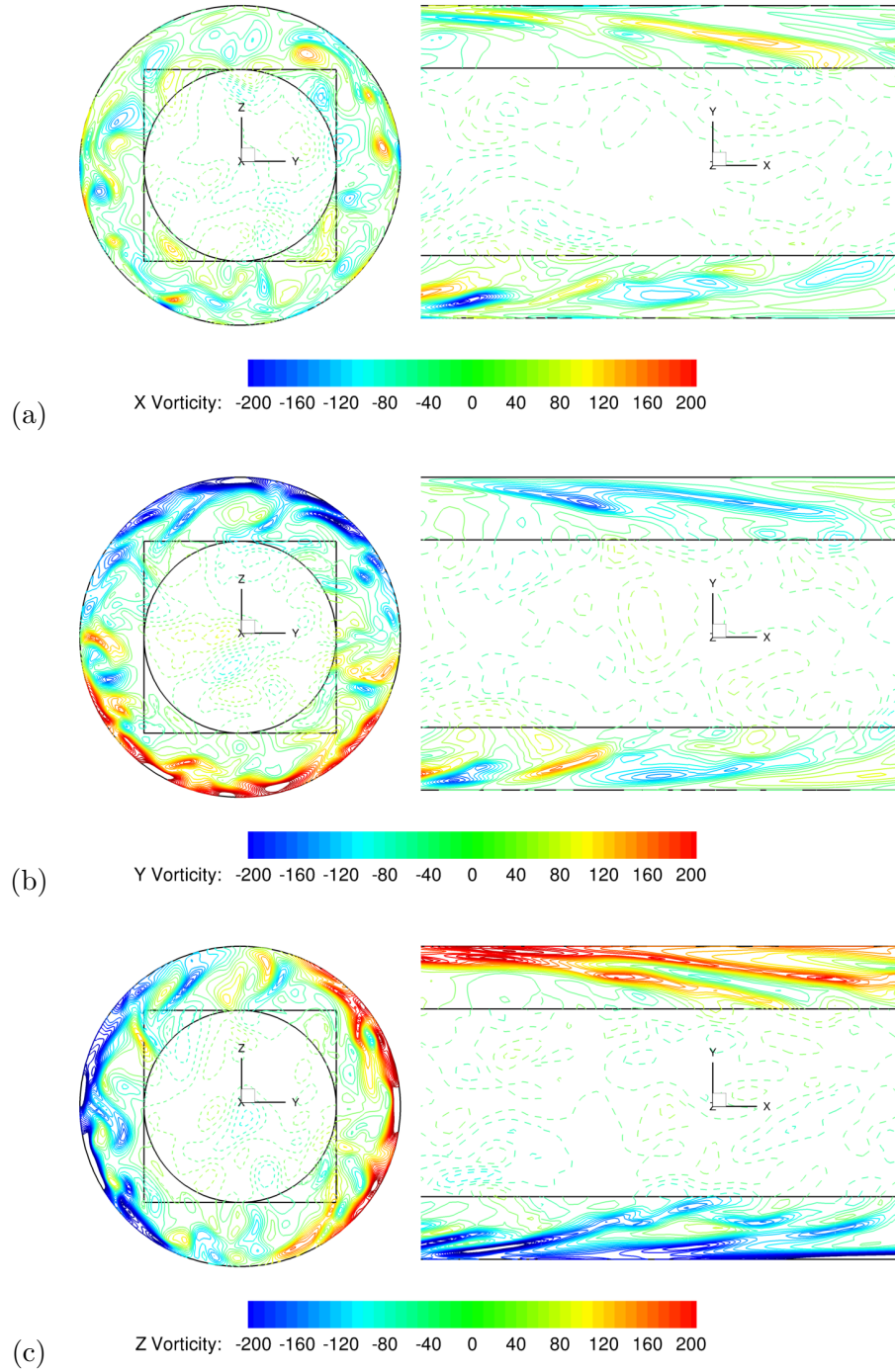


Figure 13: DNS of turbulent pipe flow on Chimera mesh: instantaneous vorticity components in cross-stream (left) and longitudinal (right) planes. Top to bottom: x-component (a), y-component (b), z-component (c).



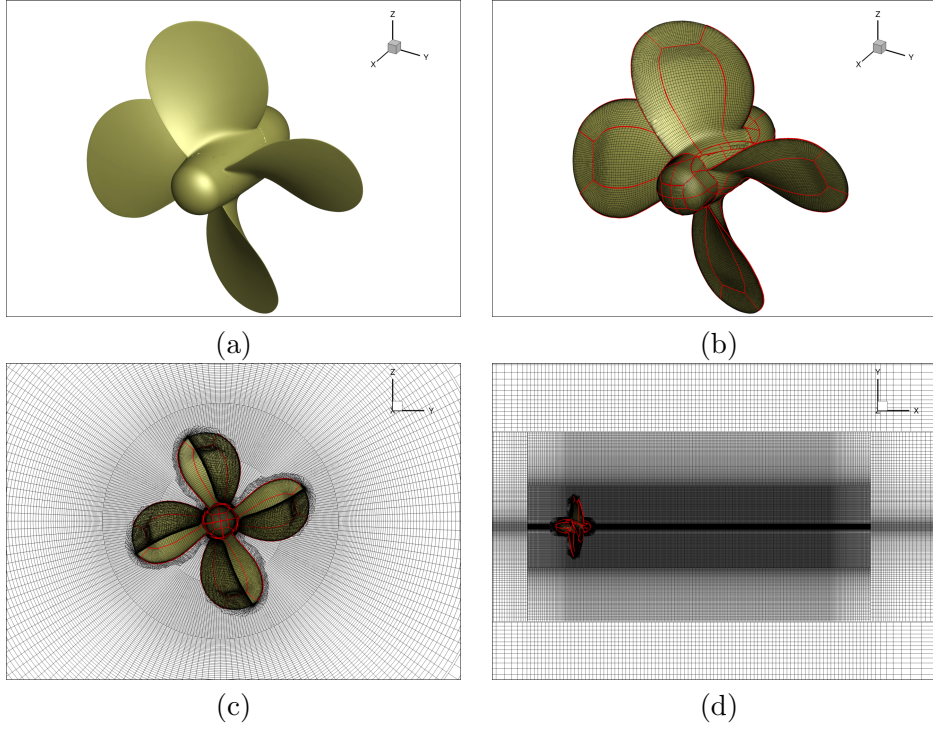


Figure 14: INSEAN propeller E779A: (a) model rendering; (b) multi-block surface grid; (c) mesh cross-section on plane  $x = 0$ ; (d) mesh cross-section on plane  $z = 0$ .

	$K_T$	$K_Q$
Med.	0.223	0.0471
Fine	0.226	0.0420
Exp.	0.221	0.0425

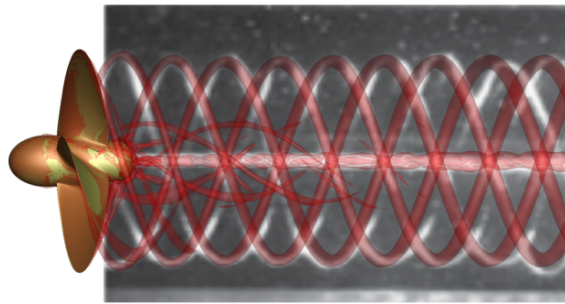


Figure 15: INSEAN propeller E779A;  $J = 0.71$ : Left: thrust and torque coefficient computed on the fine and medium grid; comparison with experimental data Felli et al. (2011). Right: Computed and observed tip vortices

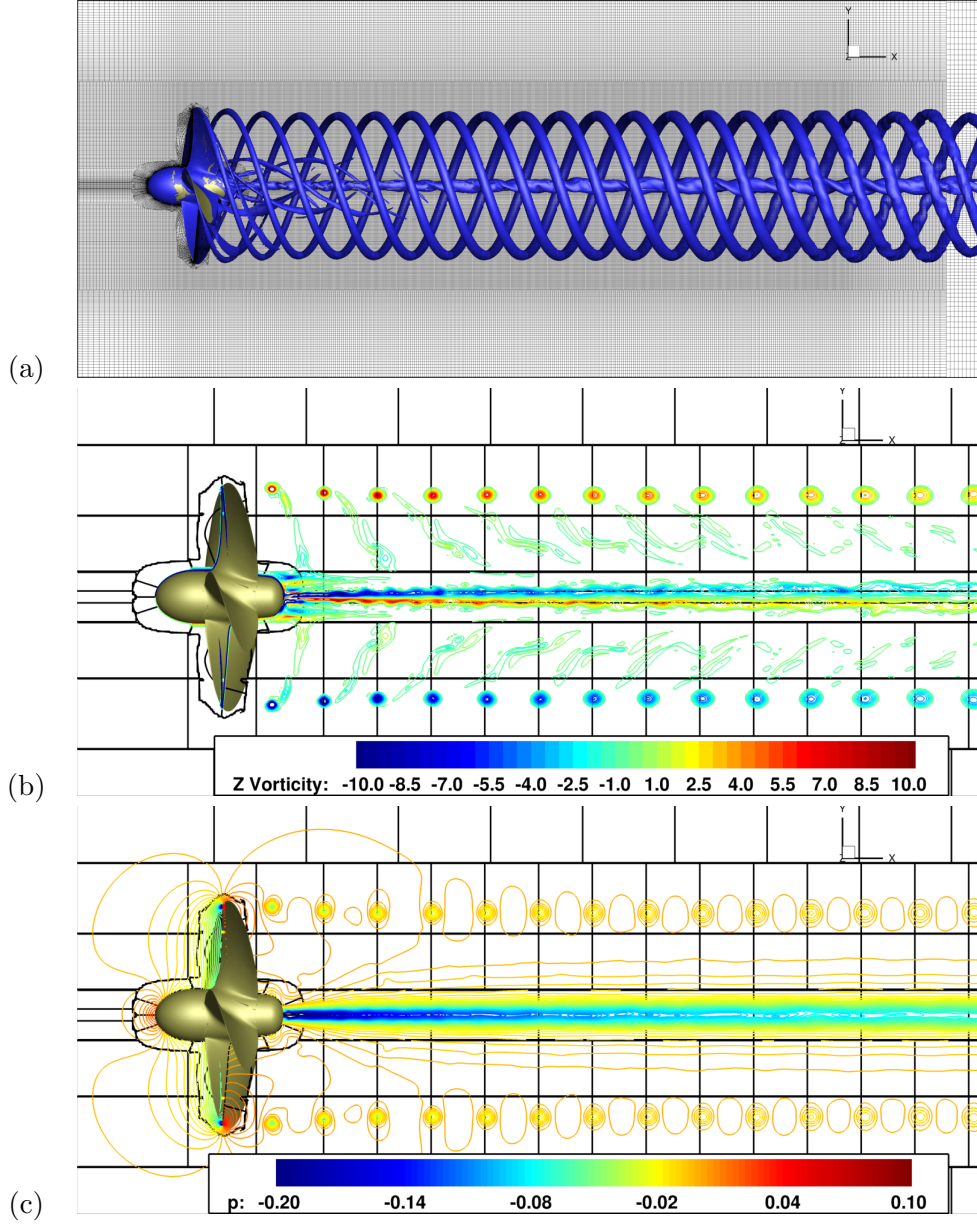


Figure 16: INSEAN propeller E779A;  $J = 0.71$ . (a) tip vortices identified by the  $\lambda_2$  criterion with  $\lambda_2 = -1$ ; (b) Z component of vorticity on the  $z=0$  plane; (c) pressure field on the  $z=0$  plane. The solid black lines denote the boundaries of the mesh blocks.



terms in the Navier-Stokes equations, enabling the discrete preservation of total kinetic energy even on smoothly distorted curvilinear meshes. Minimal filtering is applied for strongly distorted meshes to mitigate the emergence of dispersive errors that could compromise the numerical solution while preserving the formal order of accuracy of the underlying scheme. A key feature of the solver is its ability to discretely preserve free-stream properties without disturbances discretely, achieved through a three-dimensional generalization of the method proposed by Visbal and Gaitonde (2002), as detailed in A. The core of the Chimera algorithm relies on a fast and efficient donor cell search mechanism across overlapping meshes, coupled with high-accuracy interpolation schemes of up to fourth order. Information exchange between meshes is seamlessly facilitated by augmenting the Navier-Stokes equations with appropriate sponge terms, preventing the onset of spurious saw-tooth oscillations and ensuring smooth transitions across mesh interfaces.

Numerical simulations of academic benchmark problems with known analytical solutions have demonstrated that the proposed Chimera algorithm retains formal accuracy up to fourth order, even with partially overlapping meshes. We also validated the algorithm for turbulent flow in a pressure-driven pipe. Numerical results reveal no spurious oscillations in large-scale properties (e.g., velocity) or small-scale properties (e.g., vorticity), with smooth transitions across non-matching blocks. The resulting flow statistics agree with reference results obtained using standard structured solvers. To the best of our knowledge, this represents the first successful validation of DNS for turbulent flows using an overlapping mesh solver. Finally, we have applied the method to a test case relevant to marine engineering involving a rotating propeller. We performed a Detached Eddy Simulation to analyze the wake structure for this case. The properties of the numerical algorithm enable accurate prediction of the tip vortex, with its strength preserved over a significant distance downstream of the propeller hub. The numerical results show strong qualitative and quantitative agreement with available experimental data, further validating the robustness and accuracy of the proposed approach.

The method outlined in this paper opens the door for DNS, LES, and DES of turbulent flows in complex geometries, a task that the lack of efficient computational techniques for monolithic meshes has been previously limited. A key advantage of the Chimera approach is that it allows the split of the computational domain into separate, overlapping grids designed to align optimally with specific geometric features or flow regions. This flexibility allows one to generate each mesh independently, making it easier to handle complex geometries and multi-scale problems. Chimera meshes are especially valuable for problems involving moving boundaries, such as rotating blades, aircraft in flight, or fluid-structure interactions, where traditional single-mesh approaches would face significant challenges.

## Acknowledgments

This research received financial support from ICSC-Centro Nazionale di Ricerca in ‘High Performance Computing, Big Data and Quantum Computing’, funded by European Union-NextGenerationEU. The results reported in this paper have been achieved using the EuroHPC Research Infrastructure resource LEONARDO based at CINECA, Casalecchio di Reno, Italy.

## A Computation of metric tensor for uniform flow preservation

It is easy to check that in the case of a uniform flow  $\bar{\rho}, \bar{\mathbf{u}}, \bar{e}$ , equation (5) yields

$$\left[ \begin{array}{c} \bar{\rho} \bar{\mathbf{u}} \cdot \sum_{j=1}^d \sum_{\ell=1}^L a_{\ell} [(J\nabla \xi_j)_{\mathcal{N};\ell} - (J\nabla \xi_j)_{\mathcal{N};-\ell}]_{\mathcal{N}} \\ \bar{\rho} \bar{\mathbf{u}} \cdot \sum_{j=1}^d \sum_{\ell=1}^L a_{\ell} [(J\nabla \xi_j)_{\mathcal{N};\ell} - (J\nabla \xi_j)_{\mathcal{N};-\ell}]_{\mathcal{N}} + \bar{p} \sum_{j=1}^d \sum_{\ell=1}^L a_{\ell} [(J\nabla \xi_j)_{\mathcal{N};\ell} - (J\nabla \xi_j)_{\mathcal{N};-\ell}]_{\mathcal{N}} \\ \bar{\rho} \bar{H} \bar{\mathbf{u}} \cdot \sum_{j=1}^d \sum_{\ell=1}^L a_{\ell} [(J\nabla \xi_j)_{\mathcal{N};\ell} - (J\nabla \xi_j)_{\mathcal{N};-\ell}]_{\mathcal{N}} \end{array} \right] = 0. \quad (27)$$

Therefore, uniform flow preservation requires that

$$\sum_{j=1}^d \sum_{\ell=1}^L a_{\ell} [(J\nabla \xi_j)_{\mathcal{N};\ell} - (J\nabla \xi_j)_{\mathcal{N};-\ell}] = 0, \quad (28)$$

i.e., in three dimensions at  $(i, j, k)$ ,

$$\begin{aligned} \sum_{l=1}^L a_l [(J\nabla \xi)_{i+l,j,k} - (J\nabla \xi)_{i-l,j,k}] &+ \\ \sum_{m=1}^L a_m [(J\nabla \eta)_{i,j+m,k} - (J\nabla \eta)_{i,j-m,k}] &+ \\ \sum_{n=1}^L a_n [(J\nabla \zeta)_{i,j,k+n} - (J\nabla \zeta)_{i,j,k-n}] &= 0, \end{aligned} \quad (29)$$

which is a finite-difference approximation of the identity  $\partial(J\xi_{s,r})/\partial\xi_s = 0$ , with  $r = 1, 2, 3$ .

We can discretize this expression with the finite-difference approximation (3) of the exact expressions

$$J\nabla \xi_p = \frac{\varepsilon_{pqr}}{2} \frac{\partial \mathbf{x}}{\partial \xi_q} \times \frac{\partial \mathbf{x}}{\partial \xi_r}, \quad (30)$$

$\varepsilon_{pqr}$  being the Levi-Civita tensor. For instance, at  $\mathbf{x}_{i,j,k}$  one would have

$$J\nabla \xi|_{i,j,k} = \sum_{m=1}^L a_m \frac{(\mathbf{x}_{i,j+m,k} - \mathbf{x}_{i,j-m,k})}{h} \times \sum_{n=1}^L a_n \frac{(\mathbf{x}_{i,j,k+n} - \mathbf{x}_{i,j,k-n})}{h}. \quad (31)$$

Unfortunately, this approximation satisfies the identity (28) only in the two-dimensional case. For the three-dimensional case, we propose the following procedure. As suggested in Visbal and Gaitonde (2002); Sjögren et al. (2014), one can rewrite equation (30) as

$$J\nabla \xi_p = \frac{\varepsilon_{pqr}}{2} \frac{\partial \mathbf{x}}{\partial \xi_q} \times \frac{\partial \mathbf{x}}{\partial \xi_r} = \frac{\varepsilon_{pqr}}{4} \left[ \frac{\partial}{\partial \xi_r} \left( \frac{\partial \mathbf{x}}{\partial \xi_q} \times \mathbf{x} \right) - \frac{\partial}{\partial \xi_q} \left( \frac{\partial \mathbf{x}}{\partial \xi_r} \times \mathbf{x} \right) \right]. \quad (32)$$

For instance, for  $p = 1$ , one has the following expression for  $\xi_1 = \xi$

$$J\nabla \xi = \frac{1}{2} \left[ \frac{\partial}{\partial \zeta} \left( \frac{\partial \mathbf{x}}{\partial \eta} \times \mathbf{x} \right) - \frac{\partial}{\partial \eta} \left( \frac{\partial \mathbf{x}}{\partial \zeta} \times \mathbf{x} \right) \right]. \quad (33)$$

The uniform-flow preservation property in Visbal and Gaitonde (2002); Sjögren et al. (2014) extends to any order of accuracy for centered schemes if the expressions in (33) are discretized with

the finite-difference approximation (3):

$$J\nabla\xi|_{i,j,k} = \sum_{m=1}^L \sum_{n=1}^L \frac{a_m a_n}{2h^2} \{ (\mathbf{x}_{i,j+m,k+n} - \mathbf{x}_{i,j-m,k+n}) \times \mathbf{x}_{i,j,k+n} \\ - (\mathbf{x}_{i,j+m,k-n} - \mathbf{x}_{i,j-m,k-n}) \times \mathbf{x}_{i,j,k-n} \\ - (\mathbf{x}_{i,j+m,k+n} - \mathbf{x}_{i,j+m,k-n}) \times \mathbf{x}_{i,j+m,k} \\ + (\mathbf{x}_{i,j-m,k+n} - \mathbf{x}_{i,j-m,k-n}) \times \mathbf{x}_{i,j-m,k} \} . \quad (34)$$

Introducing the notation

$$\begin{aligned} \widehat{\delta_\xi^1 \mathbf{x}}_{i,j,k} &= (\mathbf{x}_{i+l,j,k} - \mathbf{x}_{i-l,j,k}) \times \mathbf{x}_{i,j,k}, \\ \widehat{\delta_\eta^{\mathbf{m}} \mathbf{x}}_{i,j,k} &= (\mathbf{x}_{i,j+m,k} - \mathbf{x}_{i,j-m,k}) \times \mathbf{x}_{i,j,k}, \\ \widehat{\delta_\zeta^{\mathbf{n}} \mathbf{x}}_{i,j,k} &= (\mathbf{x}_{i,j,k+n} - \mathbf{x}_{i,j,k-n}) \times \mathbf{x}_{i,j,k}, \end{aligned} \quad (35)$$

one can rewrite (34) as

$$J\nabla\xi|_{i,j,k} = \sum_{m=1}^L \sum_{n=1}^L \frac{a_m a_n}{2h^2} \{ \widehat{\delta_\eta^{\mathbf{m}} \mathbf{x}}_{i,j,k+n} - \widehat{\delta_\eta^{\mathbf{m}} \mathbf{x}}_{i,j,k-n} - \widehat{\delta_\zeta^{\mathbf{n}} \mathbf{x}}_{i,j+m,k} + \widehat{\delta_\zeta^{\mathbf{n}} \mathbf{x}}_{i,j-m,k} \} . \quad (36)$$

Furthermore, the first term in (29) becomes

$$\begin{aligned} \frac{\partial J\nabla\xi}{\partial\xi} \Big|_{i,j,k} &= \sum_{l=1}^L \sum_{m=1}^L \sum_{n=1}^L \frac{a_l a_m a_n}{h^3} \{ \\ &\quad \widehat{\delta_\eta^{\mathbf{m}} \mathbf{x}}_{i+l,j,k+n} - \widehat{\delta_\eta^{\mathbf{m}} \mathbf{x}}_{i+l,j,k-n} - \widehat{\delta_\zeta^{\mathbf{n}} \mathbf{x}}_{i+l,j+m,k} + \widehat{\delta_\zeta^{\mathbf{n}} \mathbf{x}}_{i+l,j-m,k} \\ &\quad - \widehat{\delta_\eta^{\mathbf{m}} \mathbf{x}}_{i-l,j,k+n} + \widehat{\delta_\eta^{\mathbf{m}} \mathbf{x}}_{i-l,j,k-n} + \widehat{\delta_\zeta^{\mathbf{n}} \mathbf{x}}_{i-l,j+m,k} - \widehat{\delta_\zeta^{\mathbf{n}} \mathbf{x}}_{i-l,j-m,k} \} . \end{aligned} \quad (37)$$

We can write the other two terms in equation (30) with  $p = 2$  and  $3$  in a similar way by index rotation

$$J\nabla\eta = \frac{1}{2} \left[ \frac{\partial}{\partial\xi} \left( \frac{\partial\mathbf{x}}{\partial\xi} \times \mathbf{x} \right) - \frac{\partial}{\partial\zeta} \left( \frac{\partial\mathbf{x}}{\partial\xi} \times \mathbf{x} \right) \right] \quad (38)$$

$$J\nabla\zeta = \frac{1}{2} \left[ \frac{\partial}{\partial\eta} \left( \frac{\partial\mathbf{x}}{\partial\xi} \times \mathbf{x} \right) - \frac{\partial}{\partial\xi} \left( \frac{\partial\mathbf{x}}{\partial\eta} \times \mathbf{x} \right) \right] \quad (39)$$

and approximate them by the same finite difference formulas as

$$J\nabla\eta|_{i,j,k} = \sum_{l=1}^L \sum_{n=1}^L \frac{a_l a_n}{2h^2} \{ \widehat{\delta_\zeta^{\mathbf{n}} \mathbf{x}}_{i+l,j,k} - \widehat{\delta_\zeta^{\mathbf{n}} \mathbf{x}}_{i-l,j,k} - \widehat{\delta_\xi^1 \mathbf{x}}_{i,j,k+n} + \widehat{\delta_\xi^1 \mathbf{x}}_{i,j,k-n} \} \quad (40)$$

and

$$J\nabla\zeta|_{i,j,k} = \sum_{l=1}^L \sum_{m=1}^L \frac{a_l a_m}{2h^2} \{ \widehat{\delta_\xi^1 \mathbf{x}}_{i,j+m,k} - \widehat{\delta_\xi^1 \mathbf{x}}_{i,j-m,k} - \widehat{\delta_\eta^{\mathbf{m}} \mathbf{x}}_{i+l,j,k} + \widehat{\delta_\eta^{\mathbf{m}} \mathbf{x}}_{i-l,j,k} \} \quad (41)$$

Then, we can rewrite the second and third terms in (29) as

$$\begin{aligned} \frac{\partial J\nabla\eta}{\partial\eta} \Big|_{i,j,k} &= \sum_{l=1}^L \sum_{m=1}^L \sum_{n=1}^L \frac{a_l a_m a_n}{h^3} \{ \\ &\quad \widehat{\delta_\zeta^{\mathbf{n}} \mathbf{x}}_{i+l,j+m,k} - \widehat{\delta_\zeta^{\mathbf{n}} \mathbf{x}}_{i-l,j+m,k} - \widehat{\delta_\xi^1 \mathbf{x}}_{i,j+m,k+n} + \widehat{\delta_\xi^1 \mathbf{x}}_{i,j+m,k-n} \\ &\quad - \widehat{\delta_\zeta^{\mathbf{n}} \mathbf{x}}_{i+l,j-m,k} + \widehat{\delta_\zeta^{\mathbf{n}} \mathbf{x}}_{i-l,j-m,k} + \widehat{\delta_\xi^1 \mathbf{x}}_{i,j-m,k+n} - \widehat{\delta_\xi^1 \mathbf{x}}_{i,j-m,k-n} \} . \end{aligned} \quad (42)$$

and

$$\begin{aligned} \left. \frac{\partial J \nabla \zeta}{\partial \zeta} \right|_{i,j,k} &= \sum_{l=1}^L \sum_{m=1}^L \sum_{n=1}^L \frac{a_l a_m a_n}{h^3} \{ \\ &\quad \widehat{\delta_{\xi}^1 \mathbf{x}}_{i,j+m,k+n} - \widehat{\delta_{\xi}^1 \mathbf{x}}_{i,j-m,k+n} - \widehat{\delta_{\eta}^{\mathbf{m}} \mathbf{x}}_{i+l,j,k+n} + \widehat{\delta_{\eta}^{\mathbf{m}} \mathbf{x}}_{i-l,j,k+n} \\ &\quad - \widehat{\delta_{\xi}^1 \mathbf{x}}_{i,j+m,k-n} + \widehat{\delta_{\xi}^1 \mathbf{x}}_{i,j-m,k-n} + \widehat{\delta_{\eta}^{\mathbf{m}} \mathbf{x}}_{i+l,j,k-n} - \widehat{\delta_{\eta}^{\mathbf{m}} \mathbf{x}}_{i-l,j,k-n} \}. \end{aligned} \quad (43)$$

If we sum all the above approximations in equation (29), we finally obtain

$$\begin{aligned} \left[ \frac{\partial J \nabla \xi}{\partial \xi} + \frac{\partial J \nabla \eta}{\partial \eta} + \frac{\partial J \nabla \zeta}{\partial \zeta} \right]_{i,j,k} &= \sum_{l=1}^L \sum_{m=1}^L \sum_{n=1}^L \frac{a_l a_m a_n}{h^3} \{ \\ &\quad \widehat{\delta_{\eta}^{\mathbf{m}} \mathbf{x}}_{i+l,j,k+n} - \widehat{\delta_{\eta}^{\mathbf{m}} \mathbf{x}}_{i+l,j,k-n} - \widehat{\delta_{\zeta}^{\mathbf{n}} \mathbf{x}}_{i+l,j+m,k} + \widehat{\delta_{\zeta}^{\mathbf{n}} \mathbf{x}}_{i+l,j-m,k} \\ &\quad - \widehat{\delta_{\eta}^{\mathbf{m}} \mathbf{x}}_{i-l,j,k+n} + \widehat{\delta_{\eta}^{\mathbf{m}} \mathbf{x}}_{i-l,j,k-n} + \widehat{\delta_{\zeta}^{\mathbf{n}} \mathbf{x}}_{i-l,j+m,k} - \widehat{\delta_{\zeta}^{\mathbf{n}} \mathbf{x}}_{i-l,j-m,k} \\ &\quad + \widehat{\delta_{\zeta}^{\mathbf{n}} \mathbf{x}}_{i+l,j+m,k} - \widehat{\delta_{\zeta}^{\mathbf{n}} \mathbf{x}}_{i-l,j+m,k} - \widehat{\delta_{\xi}^1 \mathbf{x}}_{i,j+m,k+n} + \widehat{\delta_{\xi}^1 \mathbf{x}}_{i,j-m,k+n} \\ &\quad - \widehat{\delta_{\zeta}^{\mathbf{n}} \mathbf{x}}_{i+l,j-m,k} + \widehat{\delta_{\zeta}^{\mathbf{n}} \mathbf{x}}_{i-l,j-m,k} + \widehat{\delta_{\xi}^1 \mathbf{x}}_{i,j-m,k+n} - \widehat{\delta_{\xi}^1 \mathbf{x}}_{i,j-m,k-n} \\ &\quad + \widehat{\delta_{\xi}^1 \mathbf{x}}_{i,j+m,k+n} - \widehat{\delta_{\xi}^1 \mathbf{x}}_{i,j-m,k+n} - \widehat{\delta_{\eta}^{\mathbf{m}} \mathbf{x}}_{i+l,j,k+n} + \widehat{\delta_{\eta}^{\mathbf{m}} \mathbf{x}}_{i-l,j,k+n} \\ &\quad - \widehat{\delta_{\xi}^1 \mathbf{x}}_{i,j+m,k-n} + \widehat{\delta_{\xi}^1 \mathbf{x}}_{i,j-m,k-n} + \widehat{\delta_{\eta}^{\mathbf{m}} \mathbf{x}}_{i+l,j,k-n} - \widehat{\delta_{\eta}^{\mathbf{m}} \mathbf{x}}_{i-l,j,k-n} \} \\ &\equiv 0 \end{aligned} \quad (44)$$

Therefore, if we adopt the approximation in equations (36), (40) and (41), we get the correct accuracy for the metric tensor and strictly preserve uniform flows.

## B Computation of the metric tensor on Chimera grids

The computation of the metric tensor at block boundaries with Chimera grids requires care if we want to retain the uniform flow preservation property.

To this purpose, we add  $L$  ghost cell layers on each face of each actual block. Then, on abutting block faces (with a one-to-one node matching), we simply copy the actual positions of the nodes on the adjacent block. Conversely, on natural boundaries and Chimera faces (i.e. the block faces that do not match an adjacent block face), we make a linear extrapolation of the position vector. For instance, if the ghost points  $(i, j, k)$ ,  $i = 0, -1, \dots, 1 - L$  are beyond a natural boundary or a Chimera face, and therefore  $(1, j, k)$ ,  $(2, j, k)$  are the two closest points to the boundary, we set

$$\mathbf{x}_{i,j,k} = \mathbf{x}_{1,j,k} - (1 - i)(\mathbf{x}_{2,j,k} - \mathbf{x}_{1,j,k}) \quad i = 0, -1, \dots, 1 - L \quad (45)$$

This procedure ensures that, even on highly curved concave boundaries where the grid lines are likely to intersect, equation (29) is verified. Here, of course, we must check that the sign on the Jacobian is the same  $s_J$  as for internal points: if this condition is not verified, we enforce the correct sign as  $J_{i,j,k} = s_J |J_{i,j,k}|$ .

## References

- S. Orszag, G. Patterson, Numerical simulation of three-dimensional homogeneous isotropic turbulence, *Phys. Rev. Lett.* 28 (1972) 76.
- J. Kim, P. Moin, R. Moser, Turbulence statistics in fully developed channel flow at low Reynolds number, *J. Fluid Mech.* 177 (1987) 133–166.
- S. Pirozzoli, On the streamwise velocity variance in the near-wall region of turbulent flows, *J. Fluid Mech.* 989 (2024) A5.
- S. Hosseini, R. Vinuesa, P. Schlatter, A. Hanifi, D. Henningson, Direct numerical simulation of the flow around a wing section at moderate Reynolds number, *Int. J. Heat Fluid Flow* 61 (2016) 117–128.
- J. Benek, J. Steger, F. Dougherty, A flexible grid embedding technique with application to the euler equations, in: 6th computational fluid dynamics conference Danvers, p. 1944.
- H. Pomin, S. Wagner, Navier-Stokes analysis of helicopter rotor aerodynamics in hover and forward flight, *J. Aircraft* 39 (2002) 813–821.
- A. Kravchenko, P. Moin, R. Moser, Zonal embedded grids for numerical simulations of wall-bounded turbulent flows, *J. Comput. Phys.* 127 (1996) 412–423.
- M. Vinokur, Conservation equations of gasdynamics in curvilinear coordinate systems, *J. Comput. Phys.* 14 (1974) 105–125.
- S. Pirozzoli, Stabilized non-dissipative approximations of euler equations in generalized curvilinear coordinates, *Journal of Computational Physics* 230 (2011) 2997–3014.
- A. Di Mascio, G. Dubbioso, R. Muscari, Vortex structures in the wake of a marine propeller operating close to a free surface, *Journal of Fluid Mechanics* 949 (2022) A33.
- L. Verlet, Computer "experiments" on classical fluids. I. Thermodynamical properties of Lennard-Jones molecules, *Physical Review* 159 (1967) 98.
- R. Verzicco, Immersed boundary methods: Historical perspective and future outlook, *Annual Review of Fluid Mechanics* 55 (2023) 129–155.
- J. Eggels, F. Unger, M. Weiss, J. Westerweel, R. Adrian, R. Friedrich, F. Nieuwstadt, Fully developed turbulent pipe flow: a comparison between direct numerical simulation and experiment, *J. Fluid Mech.* 268 (1994) 175–210.
- S. Pirozzoli, J. Romero, M. Fatica, R. Verzicco, P. Orlandi, One-point statistics for turbulent pipe flow up to  $Re_\tau \approx 6000$ , *J. Fluid Mech.* 926 (2021) A28.
- A. Di Mascio, R. Muscari, G. Dubbioso, On the wake dynamics of a propeller operating in drift, *Journal of fluid mechanics* 754 (2014) 263–307.
- R. Muscari, G. Dubbioso, A. Di Mascio, Analysis of the flow field around a rudder in the wake of a simplified marine propeller, *Journal of fluid mechanics* 814 (2017) 547–569.
- F. Magionesi, G. Dubbioso, R. Muscari, A. Di Mascio, Modal analysis of the wake past a marine propeller, *Journal of Fluid Mechanics* 855 (2018) 469–502.

- P. Moin, J. Kim, The structure of the vorticity field in turbulent channel flow. part 1. analysis of instantaneous fields and statistical correlations, *J. Fluid Mech.* 155 (1985) 441–464.
- M. Felli, R. Camussi, F. Di Felice, Mechanisms of evolution of the propeller wake in the transition and far fields, *Journal of Fluid Mechanics* 682 (2011) 5–53.
- R. Muscari, A. Di Mascio, R. Verzicco, Modeling of vortex dynamics in the wake of a marine propeller, *Computers & Fluids* 73 (2013) 65–79.
- P. Spalart, W. Jou, M. Strelets, S. Allmaras, Comments on the feasibility of les for wings, and on a hybrid rans/les approach. 1st afosr int, in: *Symp. Eng. Turb. Modelling and Measurements*, May, pp. 24–26.
- J. Jeong, F. Hussain, On the identification of a vortex, *Journal of fluid mechanics* 285 (1995) 69–94.
- M. R. Visbal, D. V. Gaitonde, On the use of higher-order finite-difference schemes on curvilinear and deforming meshes, *J. Comput. Phys.* 181 (2002) 155–185.
- B. Sjögren, H. C. Yee, M. Vinokur, On high order finite-difference metric discretizations satisfying gcl on moving and deforming grids, *Journal of Computational Physics* 265 (2014) 211–220.